ORIGINAL PAPER

Fabrication, experimentation and numerical simulation of micro channel heat sink for enhancing thermal performance of electronic devices

Kapil R. Aglawe[1] · Ravindra K. Yadav[1] · Sanjeev B. Thool[2]

Abstract

The reliable functioning of next-generation electronic devices within their temperature limits is contingent upon the efficient removal of high heat flux. Interfaces between the device, heat spreaders, and heat sink contribute significantly to thermal resistance in conventional chip packages. The elimination of interface resistances can lead to a noteworthy decrease in overall thermal resistance by incorporating the heat sink directly into the heat-generating device. The current study involved the manufacturing, simulation and experimentation of a micro channel heat sink. The micro channel assembly is manufactured with dimensions of $50 \times 50 \times 3$ mm. The length of micro channel is 35 mm having height and width of 0.2 mm with 58 channels. The experimentation and numerical simulation was done with considering the various parameters like mass flow rate, heat flux, and inlet temperature of nanofluid. The microchannel heat sink improved electronic device thermal performance in fabrication, experimentation, and numerical simulation. The heat sink lowered device temperatures and prevented overheating. Nanofluid at 0.3% volume and at a mass flow rate of 8 m/s, the heat transfer coefficient reaches a maximum value of 13,693.00 W/m^2 K at input temperature of 35 °C. The comprehension of the heat sink's performance was enhanced subsequent to the simulations, which unveiled the fluid flow characteristics and heat transfer mechanisms within the microchannels.

Keywords Fabrication · Numerical simulation · Microchannel heat sink · Thermal performance · Electronic devices · Computational fluid dynamics (CFD) · Thermal management

1 Introduction

The trend towards increasingly powerful and compact electronic components is leading to elevated peak and average heat fluxes that exceed the threshold at which air cooling at the board level can be considered a feasible solution [1]. Currently, there are commercial RF power amplifiers available that have dimensions smaller than one centimeter and are capable of generating heat fluxes within ranges of 1000 W/cm^2. Challenge of thermal management is intensified in situations where electronic packages are extensively integrated, due to the restricted space accessible for thermal management equipment on the board level [2, 3]. Currently,

implementation of liquid cooling by board level is a viable resolution toward the aforementioned challenges, as it has the capability to provide significantly enhanced heat transfer within limited spatial configurations [4, 5]. It is noteworthy that decreasing the size of heat transfer features and characteristic dimensions has a favorable impact on heat transfer efficiency. Nonetheless, it is important to note that there is a detrimental tension associated with hydraulic demands as the length scale decreases, as the pressure drop increases with a reduction in channel size [6]. The limitations on viable flow rates due to pressure drops in micro heat exchangers have significant implications for the sensible heating of the liquid.

Thus, it is imperative to enhance the thermal conductivity in order to address the challenges related to flow and heat transfer encountered at a microscale [7]. The limitations of coolants with constrained thermal conductivity (e.g. 0.65 W/mC) have been reached as a result of the demand for the development of more sophisticated processors [8]. Consequently, there exists a necessity to introduce a novel coolant

✉ Kapil R. Aglawe
  kapilaglawe07@gmail.com

[1] Department of Mechanical Engineering, National Institute of Technology, Raipur, Chhattisgarh 492010, India

[2] Department of Mechanical Engineering, D. J. Sanghvi College of Engineering, Mumbai, Maharashtra 400056, India

for expediting the convective cooling mechanism transpiring within the MCHS, as indicated by sources [9].

Nanofluids are classified as colloidal dispersion systems, comprising a dispersion medium (base fluid) and dispersed phase (NPs) [10–12]. The thermal conductivity of distributed nanoparticles is higher than that of a simple liquid. The production of nanofluids has been found to result in high thermal conductivity, as reported in reference [13–15]. Furthermore, the interactions involving the contact and collision of nanoparticles (NPs) [16], including those between the substrate solution and NPs, are responsible for an increase in the effective thermal conductivity of nanofluids [17, 18]. The presence of particles with dimensions ranging from millimeters to micrometers may result in wear challenges attributed to the actions of NPs, as indicated in reference [19–21]. The utilization of nanofluids as innovative refrigerants to augment heat transfer has generated considerable attention from scholars, leading to several innovative developments in the heat transfer domain [22–24].

Nanofluids are colloidal dispersion systems with a base fluid and NPs [25]. Distributed NPs carry heat better than liquids [26, 27]. Nanofluids have great thermal conductivity. NPs' interaction and collision with each other and the substrate solution increase nanofluids' effective thermal conductivity [28]. NPs may cause wear problems from millimetre and micrometre particles. Thus, scholars are interested in using nanofluids as innovative refrigerants to improve heat transmission, which has led to several new heat transfer advances [29, 30]. The manufacturing of micro channel heat sinks is broadly classified into two technologies, conventional technology and modern technology as shown in Fig. 1.

The manufacturing of micro channel heat sinks through conventional methods involves a variety of methods like micro deformation, micro milling, micro sawing, and dicing. Micro channels are formed by mechanically deforming a substrate. Cutting ceramics and glass with micro sawing is widespread [31]. Micro milling removes substrate material and shapes micro channels using rotary cutting tools. Micro deformation is a frequently employed method for materials that exhibit soft and ductile characteristics. Dicing allows for precise incisions and the creation of tiny channels with tight error margins. Material processing uses this method.

The contemporary technological advancements in the production of micro channel heat sinks have brought about a significant transformation in the process, providing sophisticated and accurate techniques for the development of effective cooling architectures. The dry etching method known as deep reactive ion etching employs plasma and reactive gases to create narrow and deep channels [32]. The process of wet etching involves submerging the substrate in a chemical solution that differentially eliminates material,

thereby creating micro channels. The process of wafer bonding involves the fusion of two or more wafers or substrates to generate miniature channels amidst them [33]. This approach allows for material flexibility and multiple functions. LIGA, an acronym for Lithography, Galvanoforming, and Molding, produces microstructures with high aspect ratios. Electro discharge machining is a non-contact method that erodes material and creates microchannels. Laser micromachining removes material and creates microchannels using high-energy laser beams. The utilization of laser micromachining facilitates the production of intricate and personalized micro channel heat sinks. Micromolding—injection molding and heat embossing—replicates micro channel architectures using molds. Modern micro channel heat sink production methods improve precision, complexity, and expandability. These structures enable customized, efficient cooling systems. They improve temperature control in electronics, aerospace, and microfluidics.

The Finite Element Method (FEM) application is utilized to simulate and analyze the mechanical behavior of 3D printed components [34, 35]. FEM is employed to numerically solve differential equations by partitioning intricate geometries into smaller, more manageable elements [36, 37]. The FEM is capable of assessing the structural integrity, deformation, and stress distribution of printed parts [38–40]. FEM is utilized to forecast the stiffness, strength, and fatigue life of a component through the process of modeling the part and assigning material properties and boundary conditions [27, 41]. The process entails the identification of areas of weakness, the optimization of design characteristics, and the selection of production parameters in order to enhance the performance of the component [42]. The utilization of FEM enables engineers and designers to conduct thorough testing on 3D-printed components prior to the prototyping or manufacturing stages [38]. The process involves the identification of locations with high levels of stress, the optimization of support structures, and the exploration of alternative designs in order to enhance the quality and functionality of the parts [43]. Finite Element Method (FEM) analysis can also provide insights into the influence of layer thickness, infill density, and printing direction on the mechanical properties of parts produced.

The employment of nanofluids for the purpose of improving thermal characteristics has emerged as a prominent area of investigation in contemporary times [44]. In laboratory trials, it was observed that the newly developed category of ultrafine nanofluid coolants exhibited promising characteristics with contrast to pure fluids [45]. The historical evolution of water cooling systems was investigated by Ellsworth et al. [46], encompassing the utilization of hybrid cooling in early IBM units and the subsequent shift towards passive water cooling. In order to provide adequate cooling capacity while ensuring ease of process on module level, the utilization of

Fig. 1 Micro channel heat sinks manufacturing technologies
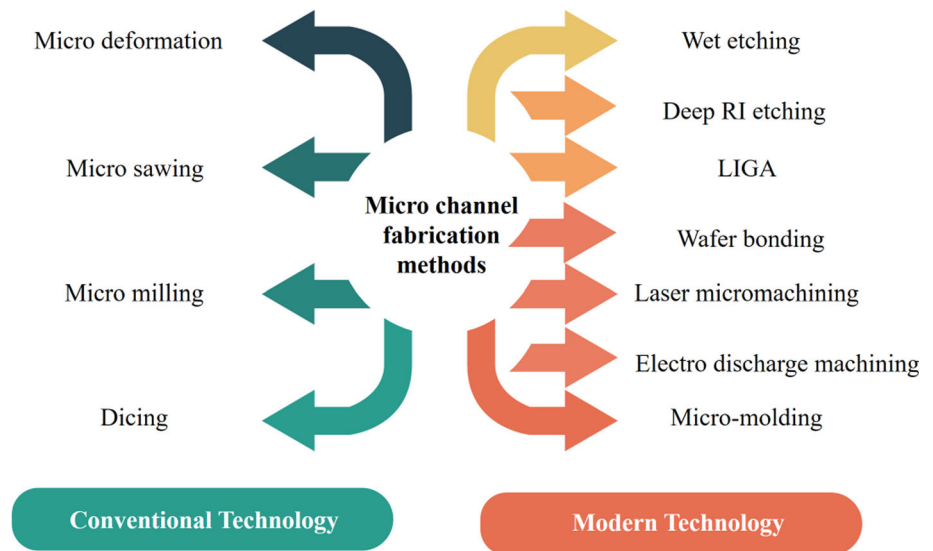
water refrigeration has been incorporated [47]. Xu et al. [48] conducted a study on analytical methods for determining heat transfer and pressure reduction in a parallel plate microchannel heat sink. The minimization of entropy production rate is achieved through the optimization of fine-geometry and flow conditions[49]. The present study concerns the constraints associated with the estimation of air conditioning through numerical modeling and the impact of heat sink. The authors Raghuraman et al. [50] performed the numerical analysis on the enhanced liquid flow properties and heat transfer behavior of rectangular microchannel heat sinks. Water was utilized as the medium of operation.

Azari et al. [51] piloted a work on the laminar convective coefficient of a nanofluid consisting of water and Al_2O_3. The work was supported out using a numerical and experimental circular tube setup, with equal surface circumstances. Ali et al. [52] worked to compare a cooling efficiency of a TiO_2 nanofluid, which was diluted to 15% under three different power inputs, specifically 125 W, 150 W, and 100 W. The results specify that the thermal efficiency of TiO_2 nanofluid is suggestively influenced by heat flow, and it can be optimized by thermal cost minimization. The study conducted by [53] examined the impact of nanofluid on the temperature of the microprocessor in the geometry sink base, with a focus on systemic effects. A cylindrical copper block was used to operate a 325-W microprocessor, and its performance was compared to that of nanofluids and heat sinks. The researchers investigated whether thermal sink geometry could safely lower microprocessor temperatures. The utilization of nanofluids in micro-pin–fin MCHS was investigated by Seyf et al. [54] through the application of numerical methods. The present study investigated the heat transfer

characteristics of MCHS. The study conducted by [55] examined the influence of NPs on the operational efficiency of a microprocessor intended for the purpose of cooling a central processing unit. Initially, distilled water was subjected to experimental and numerical analysis, followed by the examination of two different concentrations of CuO–water utilized by way of nano-fluids.

The study conducted by [56] explored a novel battery module design that utilizes a superior phase change medium consisting of two-layer nanofluids. Furthermore, the individual discovered an equation that establishes a correlation between the Nusselt number and the Richardson number. The thermal conductivity and viscosity of alumina nanofluids were examined by Shah et al. [57]. The present scheme utilizes the variable n to denote primary receptacles, m to signify individual compartments, and p to represent auxiliary vessels. Two configurations (771 and 711) were utilized to discharge each Li-ion cell under three distinct settings, as reported in reference [38]. Sultan et al. [58] conducted an investigation into the enhancement of heat transport within protruding heat sources. The study conducted by the researchers revealed that the thermal stability of Al_2O_3 nanofluid surpasses that of conventional cooling fluids. Siricharoenpanicha et al. [59] employed a blend of Ag and Fe3O4 nanofluids for the purpose of cooling. The thermal dissipation was evaluated with consideration given to the flow rate, shape, and design of the MCHS. Esmaeil et al. [60] performed experiments on mixed convection heat transfer utilizing the heat source that was cool through a pressure nanoparticle flow. The study utilized nano-silicon carbide (SiC) tubes, an aluminum chip, and paraffin wax for improving heater's efficiency [61]. The empirical results indicate

that the novel air heater functioned effectively within the climatic conditions of Baghdad. The investigation of behavior of nanofluid comprising of water and Al_2O_3 nanoparticles has been conducted by the authors cited in reference [62]. The aforementioned blend is currently being transferred into an enclosed mechanism that has been specifically engineered to facilitate the cooling of microprocessors and other electronic apparatus. Results of a study on turbulent flow demonstrate an addition of nanoparticles to a distilled fluid has a notable impact on the heat transfer rate. Furthermore, the cooling process involved the use of Glycol Ethylene, which was employed in varying volumes between 30 and 50%.

With the ongoing advancements in electronic devices, there is a corresponding increase in their complexity and functionality, resulting in the generation of elevated levels of heat. Consequently, this poses significant challenges in the effective management of maintaining optimal operating temperatures. Conventional cooling techniques, such as air cooling and traditional heat sinks, frequently prove insufficient in effectively dissipating heat from these devices, leading to diminished performance, heightened energy consumption, and potential premature failure. Hence, it is imperative to investigate alternative cooling methodologies that can augment the thermal efficiency of electronic devices. In this regard, microchannel heat sinks have emerged as a viable and promising remedy. Microchannel heat sinks provide numerous benefits compared to traditional heat sinks. These advantages encompass augmented surface area, enhanced heat transfer coefficients, and improved fluid flow characteristics. Nevertheless, a dearth of comprehensive research exists in the integration of fabrication techniques, experimental investigations, and numerical simulations to effectively enhance the design and functionality of microchannel heat sinks utilized in electronic devices.

The present investigation encompassed the fabrication, modeling, and empirical examination of a heat sink featuring micro channels. The microchannel assembly is fabricated with the specific measurements of $50 \times 50 \times 3$ mm. The micro channel under consideration measures 35 mm in length and possesses a height and width of 0.2 mm, with a total of 58 channels. The study involved conducting experimentation and numerical simulation while taking into account multiple parameters such as mass flow rate, heat flux, and inlet temperature of the nanofluid. The utilization of microchannel heat sink has been observed for enhancing a thermal performance of electronic devices in various aspects such as fabrication, experimentation, and numerical simulation. The implementation of a heat sink resulted in a reduction of device temperatures and effectively mitigated the risk of overheating. The comprehension of the heat sink's efficiency was enhanced subsequent to the simulations that exposed the microchannel fluid flow attributes and heat transfer mechanisms.

2 Materials and methods

2.1 Fabrication of micro channel heat sink

The Electrical Discharge Machining (EDM) method of fabricating microchannel heat sinks is a cutting-edge example of an advanced sort of precision technique [63]. This method combines the processes of preparing the substrate, designing and programming the process, designing and programming the electrode, performing EDM machining using electrical discharge erosion, and cooling and finishing the part. It makes it possible to create individualized cooling structures that have improved capacity for heat transfer. Electrical Discharge Machining is a precise process that enables precise control over the size of the channel, as well as complicated geometries, and it offers benefits for problematic materials. Electrical Discharge Machining necessitates the utilization of dielectric fluid for the purposes of heat dissipation and the removal of debris, which ensures the production of high-quality microchannel heat sinks. The microchannel assembly is made with precise dimensions of $50 \times 50 \times 3$ mm as shown in Fig. 2.

The microchannel arrangement is sized to maximize heat dissipation. Microchannels improve heat transfer. Each assembly microchannel is 35 mm long and 0.2 mm wide. The 35 mm coolant flow route ensures efficient heat transmission from the source. The 0.2 mm microchannel height and width balance heat exchange surface area and pressure drop. This size promotes effective fluid flow and allows for a high surface-to-volume ratio, resulting in efficient thermal performance. The microchannel assembly has 58 well-organized channels. The 58-channel microchannel assembly has a large heat dissipation surface. Figure 3a shows the fabricated microchannel whereas Microchannel assembly is shown in Fig. 3b. This arrangement enhances coolant-heated surface contact, improving heat transmission and cooling.

2.2 Experimental set up and experimentation procedure

The experimental configuration employed in the present investigation is depicted in Fig. 4. The experimental setup comprises a range of components, including a digital differential pressure transducer, coolant tank, syringe pump, thermostat, rectangular cartridge heaters, microchannel test section, computer, temperature gauge, data acquisition system, radiator, and glass wool.

Fig. 2. 2-D drawing of microchannel
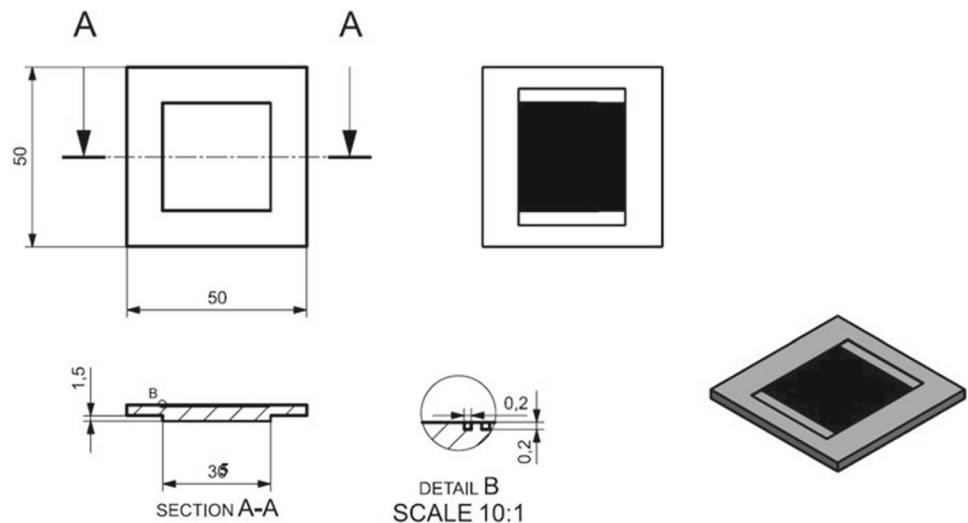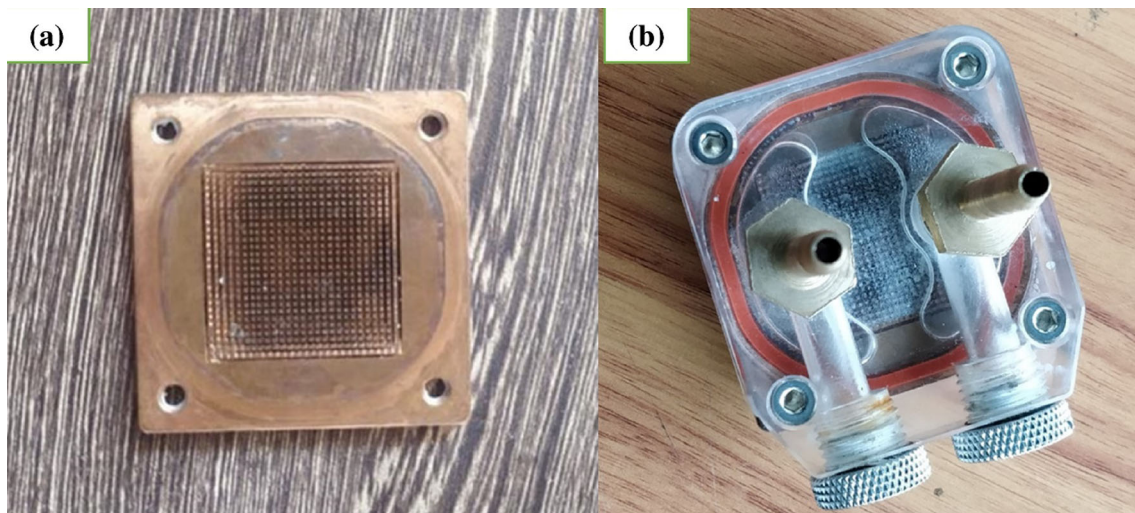
Fig. 3 **a** Fabricated microchannel, **b** microchannel assembly

The MCHS receives heat as of the rectangular cartridge heater having thickness of 1.5 mm and the capacity of 300 W, facilitated by a thermostat. This heater's heat flux ranges from 40 to 84 kW/m^2. The present study employs Al_2O_3 nanofluid at volume concentrations of 0.3%. The initial investigation involved an assessment of the permeability of the MCHS, followed by a confirmation of the efficacy of the sensors in detecting variations in temperature and pressure during the circulation of water through them. In order to maintain stability of the MFL, a regulator was employed to govern the velocity of the stepper motor [64]. The Magnetic Flux Leakage (MFL) of the fluid has been measured using a stopwatch.

The maintenance of a constant nanofluid flow rate of 0.1 LPM can be achieved through the alteration of the flow meter. The measurements for pressure and temperature were acquired under circumstances of comparative tranquility. Output was computed using the standard correlations as follows [28].

$$Q = mc(T_{\text{out}} - T_{\text{in}}) \tag{1}$$

$$N_u = h_{exp} \times \frac{D_h}{k} \tag{2}$$

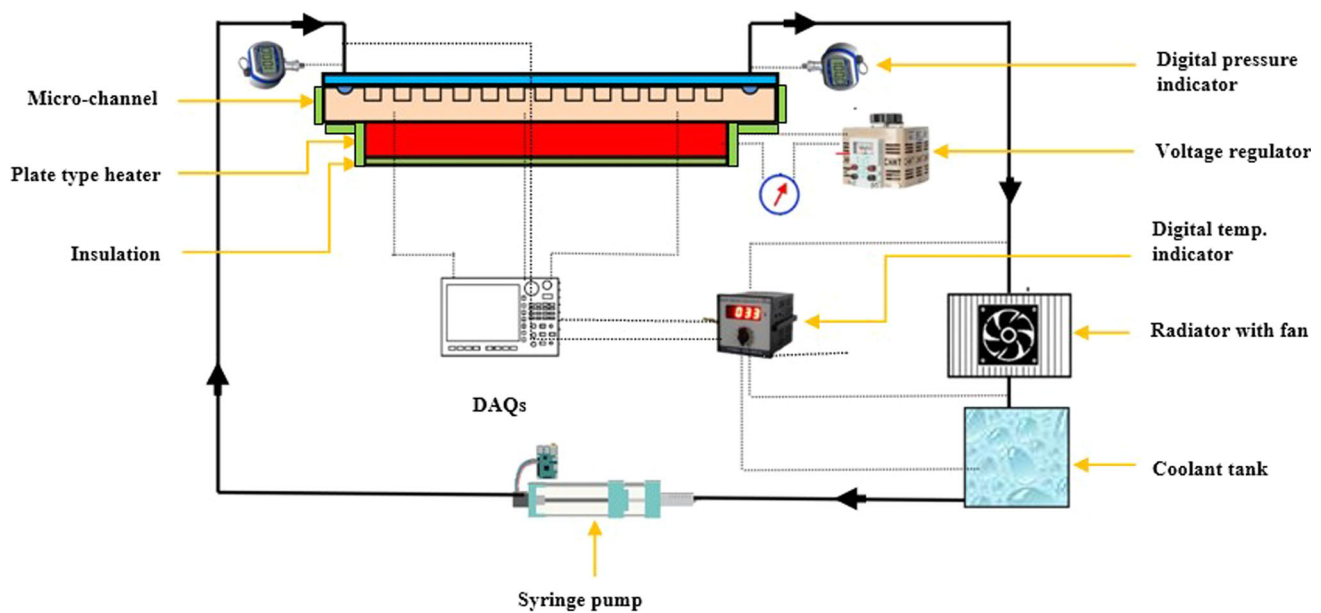$$h = Q/((T_w - T_m) \times A_s \times 58) \tag{3}$$

Fig. 4 Experimental setup block diagram

$$P_P = \Delta_P \times V_c \times 58 \times 1000 \qquad (4)$$

$$F_{\exp} = 2 * dh * \delta_P / (L * \rho * U_c^2) \qquad (5)$$

The transfer of the nanofluid from the reservoir having acrylic coolant towards MCHS examination unit was facilitated by a syringe pump. The stepper motor's regulator was employed to govern the flow rate of a nanofluid through the syringe pump. The flow rate of nanofluid is characterized by a mass flow limit (MFL) that falls within the range of 0.1–0.5 lpm. Subsequent to installation of the coolant tank and radiator, nanofluid temperature traversing a MCHS was assessed via employment of thermocouple (Ambetronics K type), which boasts the range of measurement from 0 to 3000 °C. A digital differential pressure transducer, manufactured by Setra, was affixed to both the inlet and outlet sides of an MCHS to gauge the pressure differential. The transducer is capable of measuring pressure values ranging as of 0–100Kpa.

Three additional thermocouples were installed at the base of the MCHS to monitor the temperature of its lower surface. One option is a heat sink made of copper plates that are parallel to the MCHS. The subsequent component comprises an acrylic glass layer that is placed atop the MCHS, thereby facilitating visual observation of the flow. The final component comprises a nozzle with a diameter of 2 mm, situated in an elevated position relative to the acrylic glass, facilitating the flow of nanofluid. The MCHS plate is designed with channels to facilitate the flow of nanofluid. The MCHS is equipped with a thermostat that maintains uniform heating of cartridge heater (rectangular) located on its base. Cross-flow type radiator, which is affixed to both reservoir and MCHS

test section, facilitates a cooling of the nanofluid. The computer receives the temperature of the MCHS through the data acquisition system.

2.3 Numerical simulation

The present study employs ANSYS 18.2 commercial software, to conduct a comprehensive analysis of the convective heat transfer process and fluid flow dynamics [65]. A numerical model ensuring conformity with an experimental model. This approach is preferred over a symmetric unit model. The domain of computational fluid dynamics (CFD) have expanded both upstream and downstream of a microchannel. Prior to conducting the numerical simulation, the grid independence has been evaluated. Following assumptions were taken during the modelling of the numerical solutions:

- Fluid phase was considered as a single phase.
- Steady-state flow and in compressible.
- No heat generation or viscous heating in the heat sink.Turbulent flow was considered.
- Thermal characteristics were stable throughout flow.

Figure 5 shows the various views of 3D CAD model for microchannel design in ANSYS 18.2 software in Design Modeler.

The Geometry of Microchannel consist of two part and two bodies one is the microchannel and another one is fluid domain. Fluid domain contains inlet, outlet and 58 channels. Which is shown in Figs. 6 and 7 displays the sketch map of the mesh for complete microchannel.
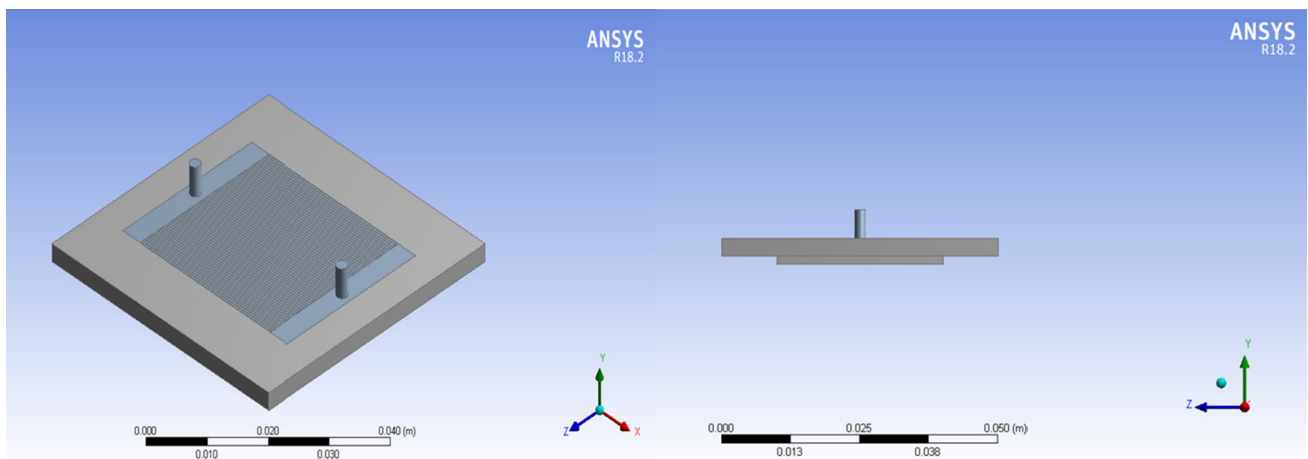
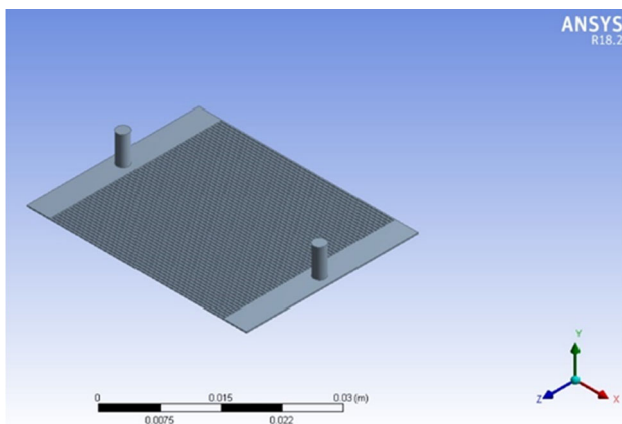**Fig. 5** Various views of 3D CAD model in design modeler

Fig. 6 displays the fluid computation domain

Governing equations on the basis of mentioned assumptions were as follows for conservation of mass, momentum, energy.

Continuity equation : $\dfrac{\text{æ}}{\text{t}} + \left(\rho \, \vec{v} \right) = 0$ \hfill (6)

Momentum equation : $\dfrac{\text{æ} \, \vec{v}}{\text{t}} + \left(\rho \, \vec{v} \, \vec{v} \right) = -\nabla P + (\tau) + \rho \, \vec{g}$ \hfill (7)

Energy equation : $\dfrac{\text{æE}}{\text{t}} + \nabla \cdot \left(\rho \, \vec{v} \, h \right) = \nabla (K \nabla T)$ \hfill (8)

The computational domain is comprised of a total of 1,253,042 individual elements and 1,328,730 number of nodes. The quantity of elements was acquired subsequent to conducting the mesh independence examination. Table 1 provided additional information regarding the characteristics of the mesh. To ensure fully developed flow, the inlet and outlet tube were chosen to have a length that is five times the diameter of the heater.

Fig. 7 Sketch map of the microchannel domain mesh
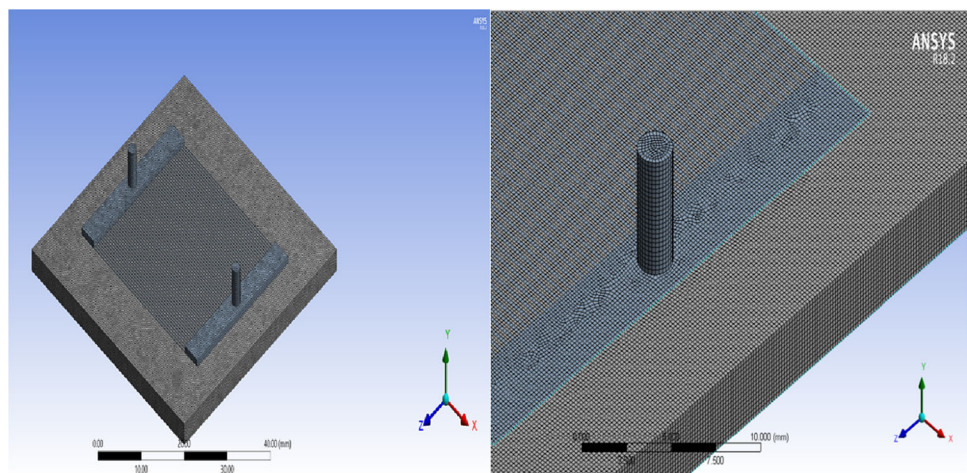
Table 1 Mesh details

| Number of Elements 1,253,042		
Number of Nodes 1,328,730		
Value	Orthogonal quality	Element quality
Min	3.8416 e−10	1.1843 e−003
Max	1	1
Average	**0.96011**	**0.95452**
Standard deviation	0.15138	0.13529

3 Results and discussion

3.1 Experimental analysis

Figure 8 depicts the alterations in convective heat transfer coefficient in relation to mass flow rate for varying inlet fluid temperatures. The heat input values of Q = 54, 74.75, and 104 W were utilized in the analysis. The intricate correlation among the heat transfer coefficient, mass flow rate, and heat input is complicated and contingent upon various factors, including but not limited to the flow regime, fluid's properties, boundary conditions and geometry of surface. The present study reveals that an increase in mass flow rate leads to an augmentation in the heat transfer coefficient. This phenomena can be explained by the thermal boundary layer becoming thicker, which improves mixing and heat transfer between the fluid and the surface. As a result, there is a tendency for the heat transfer coefficient to increase as the mass flow rate increases. At a mass flow rate of 8 m/s, the heat transfer coefficient reaches a maximum value of 13,693.00 W/m^2 K. The introduction of nanoparticles has been observed to result in an increase in the heat transfer coefficient. This phenomenon can be attributed to various factors, such as an enhancement in thermal conductivity and the presence of distinct slip mechanisms.

Figure 9 illustrates the relationship between the Nusselt number and mass flow rate for varying inlet fluid temperatures at a heat input values of Q = 54, 74.75, and 104 W. It is a widely acknowledged phenomenon that the Nusselt number experiences an upsurge with an increase in mass flow rate, as evidenced by the depicted figures. Nusselt numbers ranges from 4.1 to 4.48 for different heat input, varying mass flow rate and varying inlet temperature. At a mass flow rate of 8 ml/s, the Nusselt Numbers reaches a maximum value
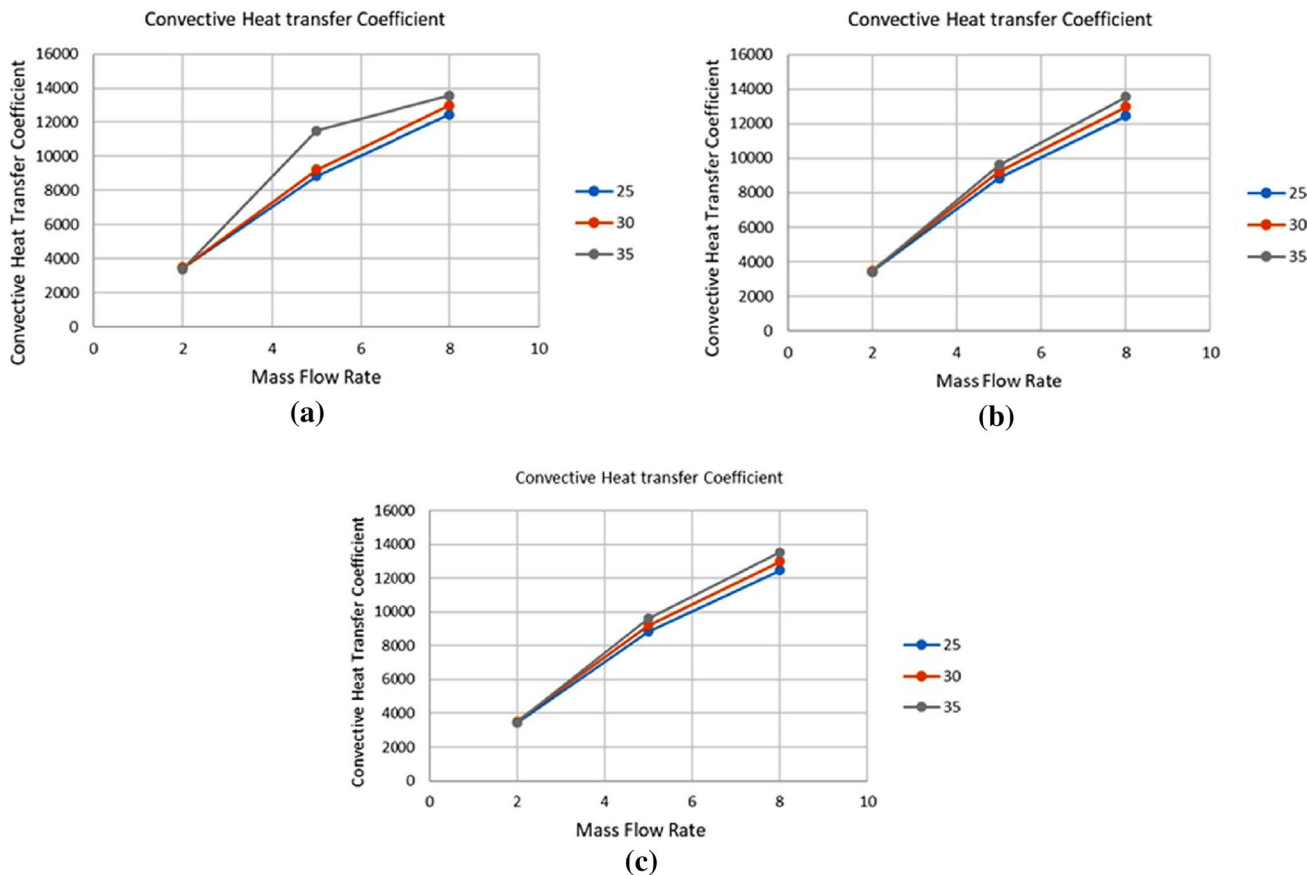
Fig. 8 Variation of heat transfer coefficient with mass flow rate **a** for Q = 54 W; **b** for Q = 74.75 W; and **c** for Q = 104 W
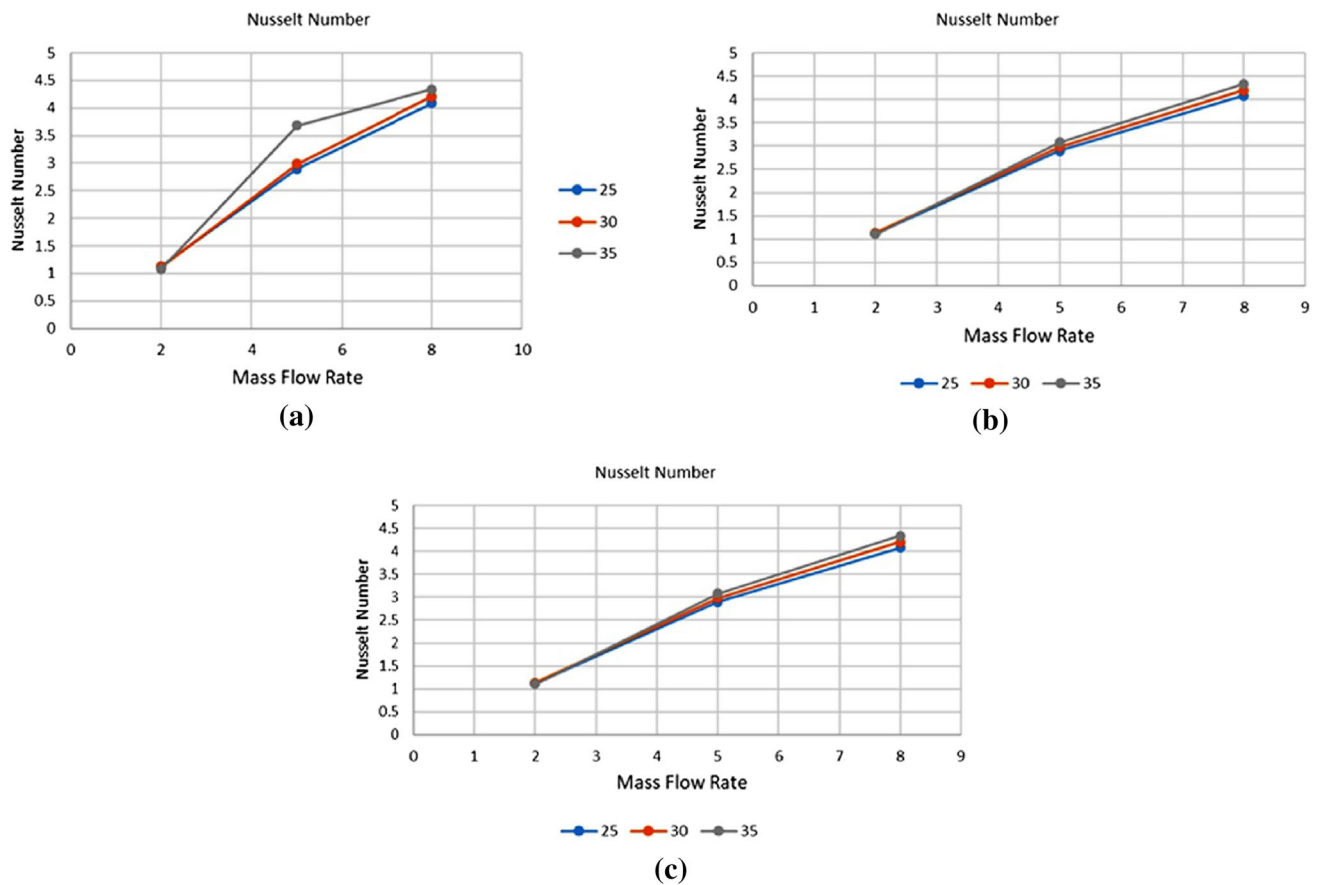
Fig. 9 Variation of Nusselt number with mass flow rate **a** for Q = 54 W; **b** for Q = 74.75 W; and **c** for Q = 104 W

of 4.28, 4.35, and 4.48 at inlet temperature of 35 °C for 54 W, 74.75 W and 104 Watt heat input. The Nusselt number's dependence on mass flow rate and varying heat inputs is contingent upon a multitude of factors, including flow regime, fluid properties, and geometry of channel. The addition of nanoparticles has been observed to result in an increase in the Nusselt number. This increase can be attributed to the corresponding increase in the heat transfer coefficient, as previously discussed. At thermal energy input elevated levels, the Nusselt coefficient shows a more pronounced escalation with augmenting mass flow rate which signifies intensification of convective heat transfer. The Nusselt number exhibits a positive correlation with the Al_2O_3, while maintaining a constant total nanoparticle volume fraction. The Nusselt number of hybrid nanofluids exhibits a significant dependence on the volume ratio of nanoparticles.

Figure 10 depicts the relationship between friction factor and mass flow rate variation inlet fluid temperatures at a heat input values of Q = 54, 74.75, and 104 W. The empirical evidence suggests that the mass flow rate exhibits an inverse relationship with the friction factor, whereas the incorporation of nanoparticles results in an escalation of the friction

factor. Friction factor ranges from 0.016 to 0.0789 for different heat input, varying mass flow rate and varying inlet temperature. At a mass flow rate of 8 ml/s, Friction factor having minimum value of 0.016 at inlet temperature of 35 °C for all heat input. The reduction in friction factor as mass flow rate increases can be attributed to the presence of laminar fluid flow within the pipe. When the heat input is held constant at 54 W, elevating the mass flow rate typically leads to augmented mass flow and which increases frictional losses which further results in an increasing friction factor. Heat affects flow regime and fluid characteristics, at 74.75 W, which may explain the non-linearity of the friction factor-mass flow rate relationship. At 104 W, increased mass flow rate and turbulence levels greatly increases the frictional losses. This phenomenon is characterized by an inverse relationship between friction factor and mass flow rate. Conversely, the introduction of nanoparticles into the fluid stream results in an increase in friction factor due to the corresponding rise in pressure drop.
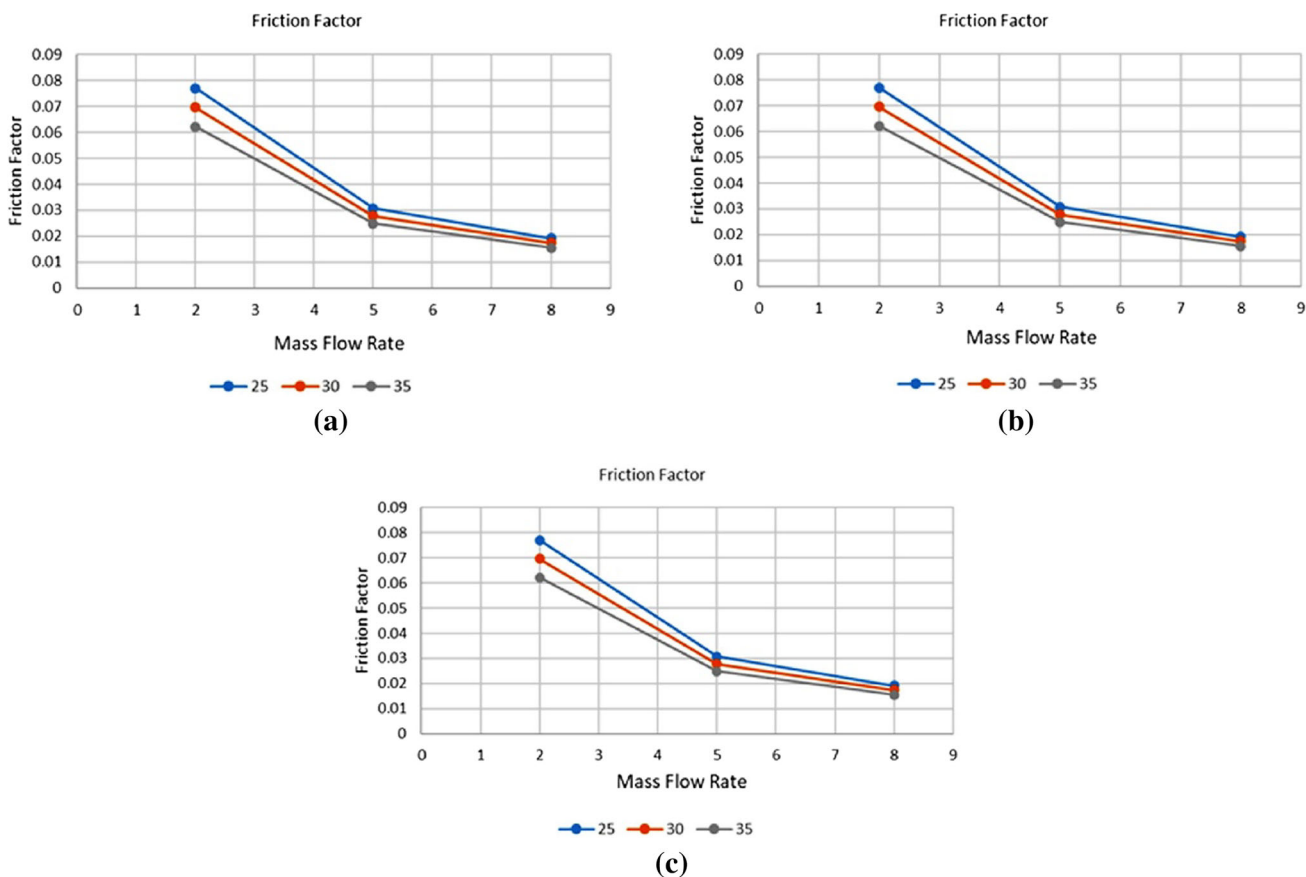
Fig. 10 Variation of friction factor with mass flow rate **a** for Q = 54 W; **b** for Q = 74.75 W; and **c** for Q = 104 W
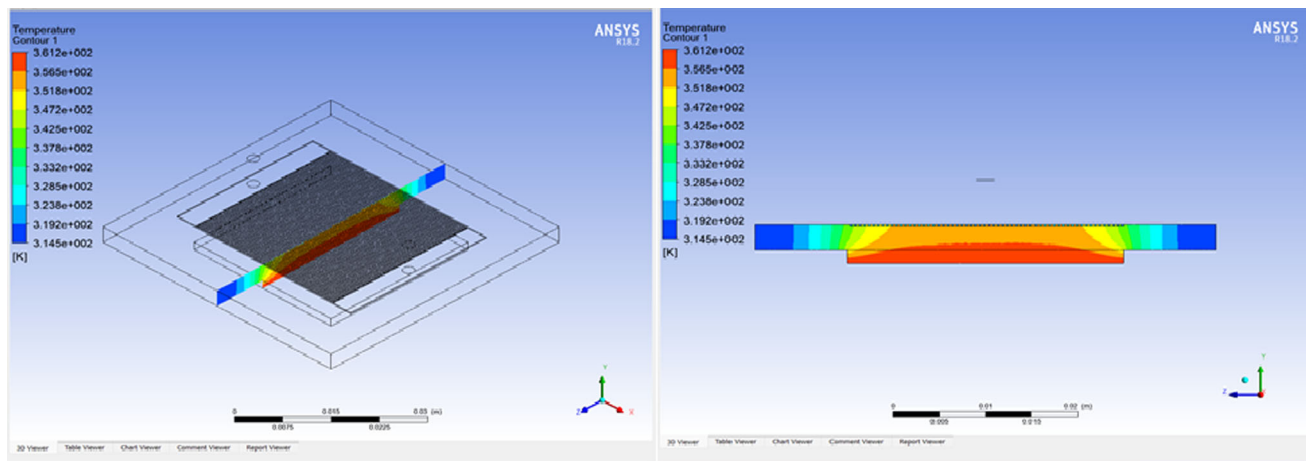

Fig. 11 Temperature distribution at the central region of a microchannel

3.2 Numerical simulation analysis

The temperature distribution at the central region of a microchannel is depicted through a contour plot in Figs. 11 with plane 1 as the focus. Temperature factors. For visualization, a YZ plane is drawn from plane 1. Any point on this central plane has a temperature of 3.565e+002 to 3.612e+002.

The temperature ranges observed within the center plane have been determined based on the results obtained from this analysis. This investigation investigated temperature changes in the plane of interest. Examining center plane temperature

ranges has revealed temperature dispersion behavior, properties, and impacts. Key elements include:

- Temperature is recorded as 3.612e+002 at the bottom of the fluid domain.
- Temperature is measured as 3.518e+002 at the top of the fluid domain.
- Temperature is found to be 3.565e+002 in the middle of the fluid domain.

The fluid region of interest is represented by the selected domain in Figs. 12, with plane 2 being the chosen specific location. The analyzed variable pertains to pressure. The pressure difference is evaluated by extending through the inlet and outlet sections to create an XY plane.

The pressure ranges observed at outlet and inlet of a microchannel have been determined based on the results obtained from this analysis. This investigation examined microchannel pressure changes, especially at its entrance and outflow. Pressure ranges have illuminated this context's pressure distribution behavior, traits, and influences. Key elements include:

- A relatively high pressure near inlet of fluid domain range from 6.823e+003 to 7.341e+003
- The outlet pressure ranges from − 4.240e+002 to 9.359e+001, indicating a lower pressure than the inlet.
- Pressure is 9.359e+001 to 7.341e+003 throughout the fluid domain. This range shows the fluid domain's pressure distribution from outlet to inlet.

Figure 13 depicts the chosen domain which denotes the fluid region that is being analyzed. The area of focus, referred to as plane 3, is specifically identified. The variable under consideration is pressure. The ZX plane is established by extending throughout the fluid domain for the purpose of assessing the pressure differential.

The pressure differences observed have been determined based on the results obtained from this analysis. The purpose of this analysis is to enhance comprehension of the fluctuations in pressure within a specific system or context. The analysis of pressure disparities has yielded significant knowledge regarding the dynamics, attributes, and consequences of alterations in pressure. The following are the key aspects that have been identified:

- The pressure difference ranges from 6.299e+003 to 7.839e+003 at the inlet which depicts a significant pressure difference between the inlet and the rest of the fluid domain.
- The pressure difference is found to be within the range of 1.169e+003 to 5.273e+003 throughout the fluid domain because of variations in pressure across the domain,

with higher pressure differences observed in certain areas.

- The pressure difference ranges from 2.708e+003 to 1.425e+002 at the outlet which depicts a relatively lower pressure difference compared to the inlet, suggesting a decrease in pressure as the fluid flows towards the outlet.

Figure 14 depicts the chosen domain, which pertains to the fluid region of interest. The designated location is identified as plane 3. The variable under consideration is temperature. The ZX plane is established by extending through the fluid domain for the purpose of assessing the temperature differential.

The temperature differences observed have been determined based on the results obtained from this analysis. The present analysis has yielded significant insights regarding the fluctuations in temperature across diverse contexts and scenarios. Several key aspects have been identified:

- The temperature ranges from 3.103e+002 to 3.140e+002 near the inlet which shows a relatively lower temperature range in the vicinity of the inlet.
- In the middle of the fluid domain, the temperature ranges from 3.140e+002 to 3.251e+002, higher than the inlet, indicating a progressive increase in temperature.
- The temperature ranges from 3.288e+002 to 3.343e+002 near the outlet indicating a further increase in temperature as the fluid approaches the outlet.

Figure 15 depicts the domain selected to encompass the entirety of the fluid region, with plane 3 being the specific location chosen for analysis. The variable under consideration pertains to velocity, whereby the velocity vector serves to denote both the direction and magnitude of fluid flow. A visualization of the velocity vector is achieved by extending an XY plane through the fluid domain.

Characteristics of the velocity vector are observed have been determined based on the results obtained from this analysis. These aforementioned characteristics offer significant insights into the behavior and properties of the velocity vector in diverse contexts.

- The velocity vector ranges from 5.038e−001 to 1.008e+000 at the inlet indicating the magnitude and direction of fluid flow entering the domain at the inlet section.
- The velocity vector ranges from 0.000e+000 to 5.038e−001 throughout the fluid domain suggesting the fluid experiences varying flow velocities within the domain, with the velocity vector indicating the direction and magnitude of fluid motion.
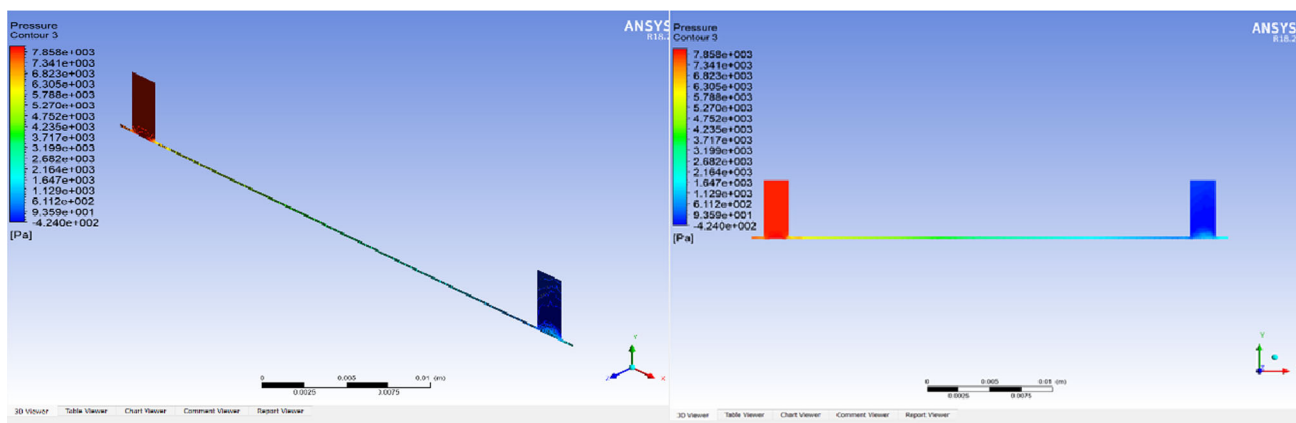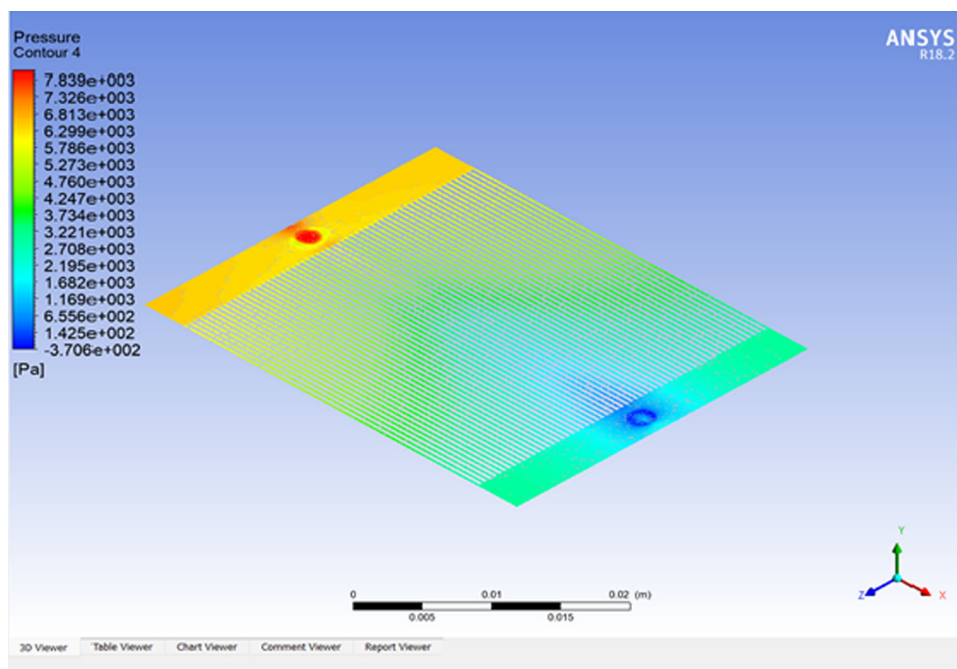- The velocity vector ranges from 1.008e+000 to 2.015e+000 at the outlet signifying the direction and

Fig. 12 Pressure difference at outlet and inlet of a microchannel

Fig. 13 Difference of pressure at inlet and outlet through the fluid domain

increased magnitude of fluid flow as it exits the domain through the outlet.

4 Conclusions

This article emphasizes the importance of microchannel heat sinks in enhancing the thermal management of electronic devices. Several significant findings and insights have been obtained through a comprehensive study that involved fabrication, experimentation, and numerical simulation.

The fabrication approach resulted in a micro channel heat sink with precisely measured dimensions and structures, greatly improving the device's ability to dissipate heat. The findings confirmed that the electronic device's thermal management was greatly improved because of micro channel heat sink's temperature maintenance and efficient heat dissipation.

The microchannel heat sink's heat transport characteristics were also modeled via numerical simulations. To better understand the heat sink's performance, these simulations shed light on the fluid flow dynamics and heat transfer mechanisms at operation. The article highlights the research outcomes that underscore the viability of micro channel heat

Fig. 14 Temperature contour throughout the fluid domain
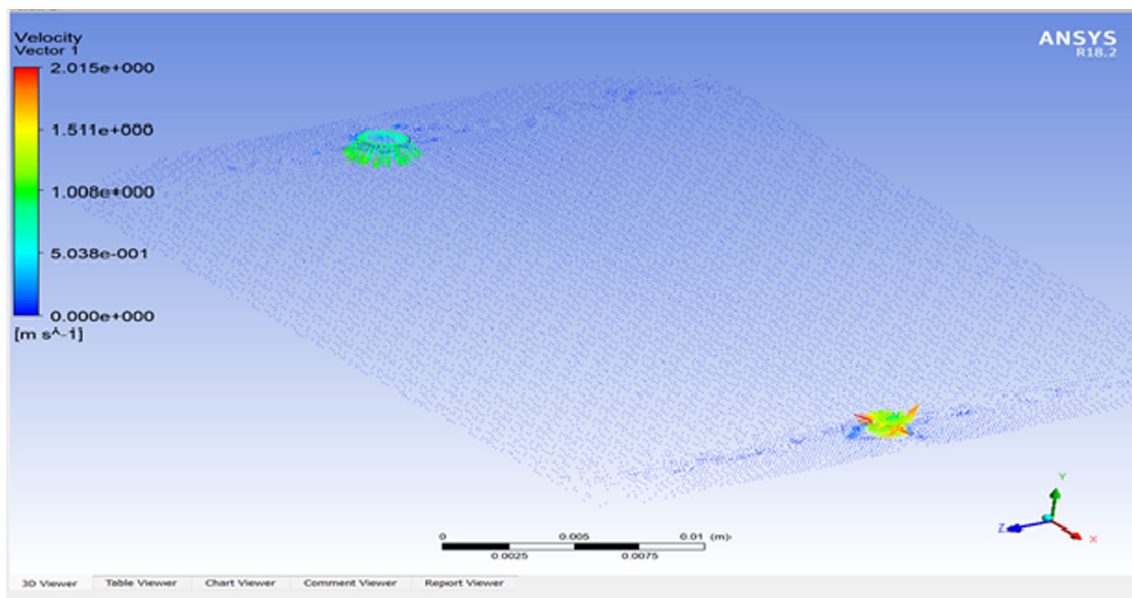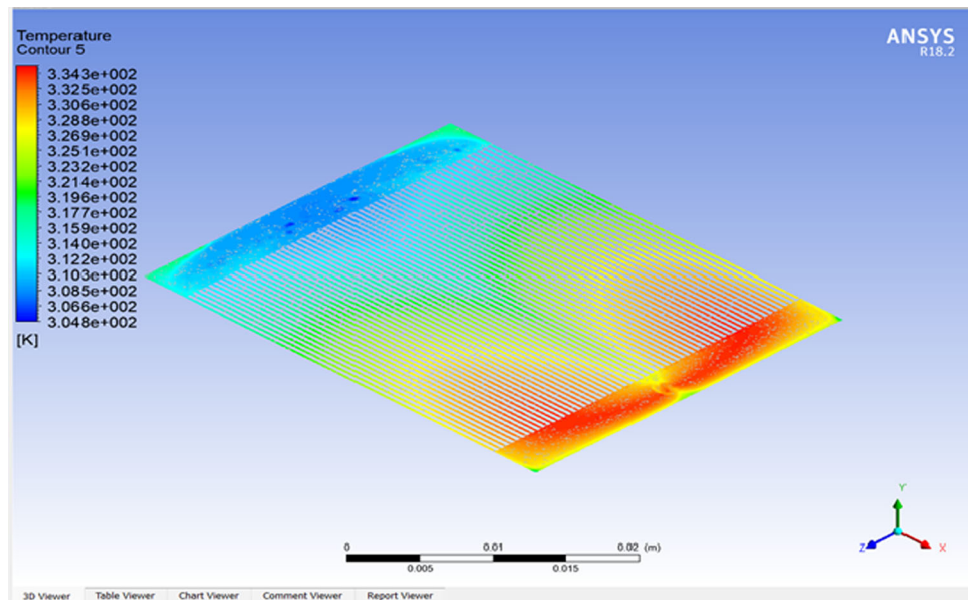
Fig. 15 Velocity vector throughout all domain

sinks as an effective and dependable cooling remedy for electronic gadgets.

Experimental and numerical studies showed that the microchannel heat sink boosted heat transfer efficiency compared to conventional cooling methods. Increased microchannel surface area, heat transfer coefficients, and convective heat transfer improve thermal performance. Through the utilization of microchannels, which improved convective heat transfer and offer augmented surface area,

these heat sinks can effectively alleviate heat-related concerns and enhance the general dependability and durability of electronic components.

Declarations

References

1. Di Capua, H.M., Escobar, R., Diaz, A.J., Guzmán, A.M.: Enhancement of the cooling capability of a high concentration photovoltaic system using microchannels with forward triangular ribs on sidewalls. Appl. Energy. **226**, 160–180 (2018). https://doi.org/10.1016/j.apenergy.2018.05.052

2. Chandrakant Nikam, K., Jathar, L., Shelare, S.D., Shahapurkar, K., Dambhare, S., Soudagar, M.E.M., Mubarak, N.M., Ahamad, T., Kalam, M.A.: Parametric analysis and optimization of 660 MW supercritical power plant. Energy **280**, 128165 (2023). https://doi.org/10.1016/j.energy.2023.128165

3. Loganathan, K., Eswaramoorthi, S., Chinnasamy, P., Jain, R., Sivasakthivel, R., Ali, R., Devi, N.N.: Heat and mass transport in Casson nanofluid flow over a 3-D riga plate with Cattaneo–Christov double flux: a computational modeling through analytical method. Symmetry **15**, 725 (2023)

4. Gorjian, A., Rahmati, E., Gorjian, S., Anand, A., Jathar, L.D.: A comprehensive study of research and development in concentrating solar cookers (CSCs): design considerations, recent advancements, and economics. Sol. Energy **245**, 80–107 (2022). https://doi.org/10.1016/j.solener.2022.08.066

5. Aglawe, K.R., Yadav, R.K., Thool, S.B.: Current technologies on electronics cooling and scope for further improvement: a typical review. In: Proceedings of the International Conference on Industrial and Manufacturing Systems (CIMS-2020), pp. 389–408. Springer (2022)

6. Jathar, L.D., Ganesan, S., Awasarmol, U., Nikam, K., Shahapurkar, K., Soudagar, M.E.M., Fayaz, H., El-Shafay, A.S., Kalam, M.A., Bouadila, S., Baddadi, S., Tirth, V., Nizami, A.S., Lam, S.S., Rehan, M.: Comprehensive review of environmental factors influencing the performance of photovoltaic panels: concern over emissions at various phases throughout the lifecycle. Environ. Pollut. **326**, 121474 (2023). https://doi.org/10.1016/j.envpol.2023.121474

7. Palande, D.D., Ghuge, N.C., Shrivastwa, R.: Comprehensive review of Karanja and Jatropha biodiesel fuelled diesel engines. Transdiscipl. J. Eng. Sci. **13**, 85–96 (2022). https://doi.org/10.22545/2022/00201

8. Jathar, L.D., Ganesan, S., Gorjian, S.: An experimental and statistical investigation of concave-type stepped solar still with diverse climatic parameters. Clean. Eng. Technol. **4**, 100137 (2021). https://doi.org/10.1016/j.clet.2021.100137

9. Bayomy, A.M., Saghir, M.Z., Yousefi, T.: Electronic cooling using water flow in aluminum metal foam heat sink: experimental and numerical approach. Int. J. Therm. Sci. **109**, 182–200 (2016). https://doi.org/10.1016/j.ijthermalsci.2016.06.007

10. Yavaş, Ö., Savran, E., Nalbur, B.E., Karpat, F.: Energy and carbon loss management in an electric bus factory for energy sustainability. Transdiscipl. J. Eng. Sci. **13**, 97–110 (2022). https://doi.org/10.22545/2022/00207

11. Jathar, L.D., Ganesan, S., Palanimuthu, L.: Performance assessment of concave-type stepped desalination unit with nanoparticles and varying water depth: an experimental approach. Int. J. Ambient Energy. **43**, 5041–5054 (2022). https://doi.org/10.1080/01430750.2021.1933589

12. Isik, Z., Bouchareb, R., Arslan, H., Özdemir, S., Gonca, S., Dizge, N., Balakrishnan, D., Prasad, S.V.S.: Green synthesis of iron oxide nanoparticles derived from water and methanol extract of *Centaurea solstitialis* leaves and tested for antimicrobial activity and dye decolorization capability. Environ. Res. **219**, 115072 (2023). https://doi.org/10.1016/j.envres.2022.115072

13. Xuan, Y., Li, Q.: Heat transfer enhancement of nanofluids. Int. J. Heat Fluid Flow. **21**, 58–64 (2000). https://doi.org/10.1016/S0142-727X(99)00067-3

14. Paul, S.C., Panda, B., Liu, J., Zhu, H.-H., Kumar, H., Bordoloi, S., Garg, A.: Assessment of flexural and splitting strength of fiber-reinforced concrete using artificial intelligence. Adv. Civ. Eng. Mater. **8**, 385–399 (2019)

15. Dadhich, Y., Alessa, N., Jain, R., Kaladgi, A.R., Loganathan, K., Devi, V.R.: Thermal onsets of viscous dissipation for radiative mixed convective flow of Jeffery nanofluid across a wedge. Symmetry **15**, 385 (2023)

16. Aglawe, K.R., Yadav, R.K., Thool, S.B.: Development of a mathematical model for prediction of heat transfer coefficient in micro-channel heat sink. Mater. Today Proc. **54**, 753–757 (2022). https://doi.org/10.1016/j.matpr.2021.11.070

17. Kumar, R., Nikam, K., Jilte, R.: A simulation model to predict coal-fired power plant production rate using artificial neural network tool. Adv. Intell. Syst. Comput. **1155**, 150–160 (2020). https://doi.org/10.1007/978-981-15-4029-5_15

18. Gajbhiye, T., Shelare, S., Aglawe, K.: Current and future challenges of nanomaterials in solar energy desalination systems in last decade. Transdiscipl. J. Eng. Sci. **13**, 187–201 (2022). https://doi.org/10.22545/2022/00217

19. Hu, Z.S., Dong, J.X.: Study on antiwear and reducing friction additive of nanometer titanium oxide. Wear **216**, 92–96 (1998). https://doi.org/10.1016/S0043-1648(97)00252-4

20. Nikam, K.C., Kumar, R., Jilte, R.: Thermodynamic modeling and performance evaluation of a supercritical coal-fired power plant situated in Western India. Energy Sour. Part A Recover. Util. Environ. Effects (2020). https://doi.org/10.1080/15567036.2020.1806410

21. Jathar, L.D., Ganesan, S.: Statistical analysis of brick, sand and concrete pieces on the performance of concave type stepped solar still. Int. J. Ambient Energy. **43**, 3727–3743 (2022). https://doi.org/10.1080/01430750.2020.1848918

22. Belkhode, P.N., Shelare, S.D., Sakhale, C.N., Kumar, R., Shanmugan, S., Soudagar, M.E.M., Mujtaba, M.A.: Performance analysis of roof collector used in the solar updraft tower. Sustain. Energy Technol. Assessments. **48**, 101619 (2021). https://doi.org/10.1016/j.seta.2021.101619

23. Sun, B., Liu, H.: Flow and heat transfer characteristics of nanofluids in a liquid-cooled CPU heat radiator. Appl. Therm. Eng. **115**, 435–443 (2017). https://doi.org/10.1016/j.applthermaleng.2016.12.108

24. Ghaffar, I., Deepanraj, B., Sundar, L.S., Vo, D.-V.N., Saikumar, A., Hussain, A.: A review on the sustainable procurement of microalgal biomass from wastewaters for the production of biofuels. Chemosphere. **311**, 137094 (2023). https://doi.org/10.1016/j.chemosphere.2022.137094

25. Shelare, S.D., Aglawe, K.R., Matey, M.S., Shelke, K.S., Sakhale, C.N.: Preparation, applications, challenges and future prospects of nanofluid materials with a solar systems in the last decade. Mater. Today Proc. (2023). https://doi.org/10.1016/j.matpr.2023.06.160

26. Nikam, K.C., Kumar, R., Jilte, R.: Economic and exergoeconomic investigation of 660 MW coal-fired power plant. J. Therm. Anal. Calorim. (2020). https://doi.org/10.1007/s10973-020-10213-z

27. Shelare, S., Kumar, R., Gajbhiye, T., Kanchan, S.: Role of geothermal energy in sustainable water desalination—a review on current status, parameters, and challenges. Energies **16**, 2901 (2023). https://doi.org/10.3390/en16062901

28. Aglawe, K., Yadav, R., Thool, S.: Experimental Investigation of Al2O3 Nanofluid for Thermal Energy Management of Microchannel Heat Sink. Transdiscipl. J. Eng. Sci. **13**, 203–216 (2022). https://doi.org/10.22545/2022/00218

29. Nikam, K.C., Kumar, R., Jilte, R.: Exergy and exergo-environmental analysis of a 660 MW supercritical coal-fired power plant. J. Therm. Anal. Calorim. (2020). https://doi.org/10.1007/s10973-020-10268-y

30. Nikam, K., Kumar, R., Jilte, R.: Exergy Analysis of a 660 MW thermal power plant bt - recent trends in thermal engineering. (2022)

31. Shelare, S., Belkhode, P., Nikam, K.C., Yelamasetti, B., Gajbhiye, T.: A payload based detail study on design and simulation of hex-acopter drone. Int. J. Interact. Des. Manuf. (2023). https://doi.org/10.1007/s12008-023-01269-w

32. Shelare, S.D., Aglawe, K.R., Waghmare, S.N., Belkhode, P.N.: Advances in water sample collections with a drone—a review. Mater. Today Proc. **47**, 4490–4494 (2021). https://doi.org/10.1016/j.matpr.2021.05.327

33. Aglawe, K.R., Dhande, M., Matey, M., Shelare, S.: State of the art and materials based characteristics in power converters for electric vehicles. Mater. Today Proc. **58**, 726–735 (2022). https://doi.org/10.1016/j.matpr.2022.02.384

34. Yelamasetti, B., Manikyam, S., Kumar, R., Saxena, K.K.: Finite element simulation for predicting temperature and residual stresses distribution developed in dissimilar welds of Monel 400 and AISI 309L. Adv. Mater. Process. Technol. **8**, 1206–1216 (2022). https://doi.org/10.1080/2374068X.2021.1948702

35. Shelare, S.D., Aglawe, K.R., Khope, P.B.: Computer aided modeling and finite element analysis of 3-D printed drone. Mater. Today Proc. **47**, 3375–3379 (2021). https://doi.org/10.1016/j.matpr.2021.07.162

36. Yelamasetti, B., Ramana, G.V., Manikyam, S., Vardhan, T.V.: Thermal field and residual stress analyses of similar and dissimilar weldments joined by constant and pulsed current TIG welding techniques. Adv. Mater. Process. Technol. **8**, 1889–1904 (2022). https://doi.org/10.1080/2374068X.2021.1959114

37. Ambade, S.P., Tembhurkar, C.K., Shelare, S., Gupta, S.: Application of ANN and Taguchi technique for material removal rate by abrasive jet machining with special abrasive materials. In: Evolutionary Optimization of Material Removal Processes, pp. 97–128. CRC Press, Boca Raton (2022)

38. Sahu, P., Shelare, S., Sakhale, C.: Smart cities waste management and disposal system by smart system: a review. Int. J. Sci. Technol. Res. **9**, 4467–4470 (2020)

39. Yelamasetti, B., Ramana, G.V., Sanke, N., Gupta, N.: Numerical and experimental residual stress analysis of dissimilar metals of Inconel 718 and AISI 316 developed in GTAW process. Int. J. Interact. Des. Manuf. (2022). https://doi.org/10.1007/s12008-022-00932-y

40. Shelare, S.D., Thakare, P.S., Handa, C.C., Professor, A.: Computer aided modelling and position analysis of crank and slotted lever mechanism. Int. J. Mech. Prod. Eng. Res. Dev. **2**, 47–52 (2012)

41. Yelamasetti, B., Vemanaboina, H.: Comparison of metallurgical and mechanical properties of dissimilar joint of AISI 316 and Monel 400 developed by pulsed and constant current gas tungsten arc welding processes. Int. J. Adv. Manuf. Technol. **108**, 2633–2644 (2020). https://doi.org/10.1007/s00170-020-05562-w

42. Khope, P.B., Shelare, S.D.: Prediction of torque and cutting speed of pedal operated chopper for silage making. In: Lecture Notes in Mechanical Engineering, pp. 243–249. Springer (2021)

43. Naidu, V.A.M., et al.: A review on design of components of stroke engine using hybrid metal matrix. Int. J. Mech. Prod. Eng. Res. Dev. **10**, 8853–8862 (2020). https://doi.org/10.24247/ijmperdjun2020842

44. Gajbhiye, T.S., Waghmare, S.N., Sirsat, P.M., Borkar, P., Awatade, S.M.: Role of nanomaterials on solar desalination systems: a review. Mater. Today Proc. (2023). https://doi.org/10.1016/j.matpr.2023.04.532

45. Kamyar, A., Saidur, R., Hasanuzzaman, M.: Application of computational fluid dynamics (CFD) for nanofluids. Int. J. Heat Mass Transf. **55**, 4104–4115 (2012). https://doi.org/10.1016/j.ijheatmasstransfer.2012.03.052

46. Ellsworth, M.J., Campbell, L.A., Simons, R.E., Iyengar, M.K., Schmidt, R.R., Chu, R.C.: The evolution of water cooling for IBM large server systems: back to the future. In: 2008 11th IEEE inter-society conference on thermal and thermomechanical phenomena in electronic systems, I-THERM, pp. 266–274 (2008)

47. Model, C.E.: Exploring grassroots renewable energy transitions: developing a community-scale energy model. Transdiscipl. J. Eng. Sci. **2**, 137–163 (2022). https://doi.org/10.22545/2022/00215

48. Xu, G., Guenin, B., Vogel, M.: Extension of air cooling for high power processors. Thermomech. Phenom. Electron. Syst. Proc. Intersoc. Conf. **1**, 186–193 (2004). https://doi.org/10.1109/itherm.2004.1319172

49. Jain, A., Bora, B.J., Kumar, R., Sharma, P., Deepanraj, B., Irshad, K., Ravikiran, C.: Application of hybrid Taguchi L16 and desirability for model prediction and optimization in assessment of the performance of a novel Water Hyacinth biodiesel run diesel engine. Fuel. **339**, 127377 (2023). https://doi.org/10.1016/j.fuel.2022.127377

50. Raghuraman, D.R.S., Thundil-Karuppa-Raj, R., Nagarajan, P.K., Rao, B.V.A.: Influence of aspect ratio on the thermal performance of rectangular shaped micro channel heat sink using CFD code. Alex. Eng. J. **56**, 43–54 (2017). https://doi.org/10.1016/j.aej.2016.08.033

51. Azari, A., Kalbasi, M., Rahimi, M.: CFD and experimental investigation on the heat transfer characteristics of alumina nanofluids under the laminar flow regime. Braz. J. Chem. Eng. **31**, 469–481 (2014). https://doi.org/10.1590/0104-6632.20140312s00001959

52. Ali, H.M., Arshad, W.: Effect of channel angle of pin-fin heat sink on heat transfer performance using water based graphene nanoplatelets nanofluids. Int. J. Heat Mass Transf. **106**, 465–472 (2017). https://doi.org/10.1016/j.ijheatmasstransfer.2016.08.061

53. Jajja, S.A., Ali, W., Ali, H.M., Ali, A.M.: Water cooled minichannel heat sinks for microprocessor cooling: effect of fin spacing. Appl. Therm. Eng. **64**, 76–82 (2014). https://doi.org/10.1016/j.applthermaleng.2013.12.007

54. Seyf, H.R., Feizbakhshi, M.: Computational analysis of nanofluid effects on convective heat transfer enhancement of micro-pin-fin heat sinks. Int. J. Therm. Sci. **58**, 168–179 (2012). https://doi.org/10.1016/j.ijthermalsci.2012.02.018

55. Al-Rashed, M.H., Dzido, G., Korpyś, M., Smołka, J., Wójcik, J.: Investigation on the CPU nanofluid cooling. Microelectron. Reliab. **63**, 159–165 (2016). https://doi.org/10.1016/j.microrel.2016.06.016

56. Jilte, R., Afzal, A., Panchal, S.: A novel battery thermal management system using nano-enhanced phase change materials. Energy. **219**, 119564 (2021). https://doi.org/10.1016/j.energy.2020.119564

57. Shah, J., Ranjan, M., Davariya, V., Gupta, S.K., Sonvane, Y.: Temperature-dependent thermal conductivity and viscosity of synthesized α-alumina nanofluids. Appl. Nanosci. **7**, 803–813 (2017). https://doi.org/10.1007/s13204-017-0594-7

58. Sultan, G.I.: Enhancing forced convection heat transfer from multiple protruding heat sources simulating electronic components in a horizontal channel by passive cooling. Microelectron. J. **31**, 773–779 (2000). https://doi.org/10.1016/S0026-2692(00)00058-6

59. Siricharoenpanich, A., Wiriyasart, S., Srichat, A., Naphon, P.: Thermal cooling system with Ag/Fe$_3$O$_4$ nanofluids mixture as coolant for electronic devices cooling. Case Stud. Therm. Eng. **20**, 100641 (2020). https://doi.org/10.1016/j.csite.2020.100641

60. Esmaeil, K.K., Sultan, G.I., Al-Mufadi, F.A., Almasri, R.A.: Experimental heat transfer from heating source subjected to rigorous natural convection inside enclosure and cooled by forced nanofluid flow. J. Heat Transf. (2019). https://doi.org/10.1115/1.4043673

61. Jawad, Q.A., Mahdy, A.M.J., Khuder, A.H., Chaichan, M.T.: Improve the performance of a solar air heater by adding aluminum chip, paraffin wax, and nano-SiC. Case Stud. Therm. Eng. **19**, 100622 (2020). https://doi.org/10.1016/j.csite.2020.100622

62. Nguyen, C.T., Desgranges, F., Roy, G., Galanis, N., Maré, T., Boucher, S., Angue Mintsa, H.: Temperature and particle-size

dependent viscosity data for water-based nanofluids—hysteresis phenomenon. Int. J. Heat Fluid Flow. **28**, 1492–1506 (2007). https://doi.org/10.1016/j.ijheatfluidflow.2007.02.004

63. Kumar Yadav, A., Agrawal, M.K., Saxena, K.K., Yelamasetti, B.: Prediction of thermal fields and stresses developed in GTAW dissimilar weldments of AA 5083 and AA 6082. Mater. Today Proc. (2023). https://doi.org/10.1016/j.matpr.2023.03.174

64. Bridjesh, P., Geetha, N.K., Yelamasetti, B.: Numerical investigation on buckling of two-directional porous functionally graded beam using higher order shear deformation theory. Int. J. Interact. Des. Manuf. (2023). https://doi.org/10.1007/s12008-023-01332-6

65. Yadav, A.K., Agrawal, M.K., Saxena, K.K., Yelamasetti, B.: Numerical simulation and experimental residual stress analyses of dissimilar GTA weldments of AA 5083 and AA 6082. Int. J. Interact. Des. Manuf. (2023). https://doi.org/10.1007/s12008-023-01216-9